CrossMark

ORIGINAL PAPER

Effect of Wheel Speed on the Structure, Microstructure, Magnetic, and Electrical Properties of Tb-Fe-Co Ribbons

K. Umadevi[1,2] · Mithun Palit[1] · J. Arout Chelvane[1] · D. Arvindha Babu[1] ·
A. P. Srivastava[3] · S. V. Kamat[1] · V. Jayalakshmi[2]

Abstract Melt spun ribbons of Tb-Fe-Co alloy made with different speeds, viz., 15, 25, 34, and 47 m/s were investigated for structural, microstructural, magnetic, and electrical properties. High cooling rates achieved during melt spinning process were found to significantly affect the microstructure of Tb-Fe-Co ribbons. Structural investigations employing X-ray diffraction and transmission electron microscopy for the Tb-Fe-Co ribbons showed the presence of BCC Fe-Co and amorphous Tb-Fe-Co phases coexisting with the crystalline Tb-Fe-Co phase which has a C15-type cubic Laves structure. In addition, the average grain size of the crystalline Tb-Fe-Co phase is found to decrease with increasing wheel speed during melt spinning. A coercivity value as high as 3.3 kOe was obtained for the melt spun ribbon prepared at 47 m/s wheel speed whereas the as-cast alloy exhibited a coercivity value around 300 Oe. This was attributed to the reduction in the grain size of the crystalline Tb-Fe-Co phase upon melt spinning. Temperature-dependent resistivity measurements indicated that both the as-cast and melt spun ribbons were metallic in nature. The low-temperature resistivity which is dominated by electron-magnon scattering component for the as-cast and melt spun ribbon prepared at 15 m/s was found to show electron-electron scattering as the predominant mechanism with an increase in wheel speed.

Keywords Melt spun ribbons · Magnetization measurements · Microstructural investivations

✉ J. Arout Chelvane
aroutchelvane@gmail.com

1 Defence Metallurgical Research Laboratory, Hyderabad, India

2 Department of Physics, National Institute of Technology Warangal, Warangal, India

3 Bhabha Atomic Research Centre, Mumbai, India

1 Introduction

Extensive studies on Tb-Fe-Co thin films have been carried out by several researchers during the past few decades due to its potential applications in the field of sensors, actuators, and magneto-optical recording media etc. [1–3]. This multifunctionality stems from the various interesting properties exhibited by these films such as large magnetostriction, domain wall pinning, perpendicular magnetic anisotropy (PMA), tunable magnetization and coercivity, and large thermal stability [4–11]. These properties were found to be highly dependent on Tb to (Fe-Co) ratio [12]. Although this material was initially considered for magneto-optical recording applications, the current interest is more inclined towards utilizing it as a potential electrode material for second-generation spintronics devices such as spin transfer torque random access memory owing to their large thermal stability and tunable magnetic properties [13–15]. Further, these tunable properties also make them suitable for exchange-spring magnets. Attempts were made to develop such exchange-spring magnets by growing Tb-Fe-Co/Fe multilayers to achieve large magnetization and coercivity [16]. Although considerable progress has been made to exploit this material for device-level applications, the physics behind the origin of perpendicular magnetic anisotropy and its impact on the achieved coercivity is still elusive. Existing literature on this material system suggests the presence of columnar structure,

ordering of rare earth ions, stress-induced anisotropy, and formation of nano-crystalline phases as reasons for the origin of PMA in Tb-Fe-Co-based films [17–19]. In addition, several studies were also carried out to understand the PMA by varying the substrate-related parameters such as (i) materials (Si, SiO, glass, etc.), (ii) orientation, (iii) temperature, and (iv) buffer layer material (Ta, Al, Ag, etc.) [6, 8, 20–24]. However, none of these experiments yielded a strong conclusive evidence for PMA owing to the amorphous nature of Tb-Fe-Co films. Recently, we have studied the effect of rapid thermal annealing on the microstructure and the magnetic properties of amorphous Tb-Fe-Co thin films [6]. Evolution of phases with heat treatment was found to have a profound impact on the PMA. However, complete crystallization of the film could not be achieved owing to the onset of formation of reaction on products at the film-substrate interface prior to complete crystallization. Therefore, it would be of interest to understand the evolution of these phases and their effect on PMA in the absence of any substrate. Melt spinning is a non-equilibrium rapid solidification process where very high cooling rates are achieved similar to thin film processing. During rapid solidification process, free-standing ribbons can be obtained with varying microstructures based on the solidification rates employed during melt spinning. In this context, a study has been taken up to produce free-standing Tb-Fe-Co ribbons with varying wheel speeds and investigate their structure, microstructure, magnetic properties, and electrical resistivity.

2 Experimental Details

The alloy with a composition of $Tb(Fe_{0.55}Co_{0.45})_{1.75}$ was prepared by induction melting and casting under vacuum high-purity elements (purity better than 99.95 %) which were used for this purpose. Rapidly solidified ribbons of this alloy were prepared by employing a vacuum melt spinner capable operating at different wheel speeds, viz., 15, 25, 34, and 47 m/s. Structural characterization was carried out using an X-ray diffractometer employing Cu-$K\alpha$ radiation. Transmission electron microscope (TEM) was used for investigating the microstructure of rapidly solidified alloy ribbons, respectively. Room temperature and low temperature magnetization measurements were carried out using a vibrating sample magnetometer and SQUID magnetometer up to a maximum magnetic field of 60 kOe. Demagnetization field correction was made for the magnetization measured along the out-of-plane magnetization. The resistivity measurements were carried out on the as-cast alloy and alloy ribbons employing a linear four-probe technique in the temperature range of 10–300 K using a constant current source and nano-voltmeter.

3 Results and Discussions

The composition of the alloy selected for the study, viz., $Tb(Fe_{0.55}Co_{0.45})_{1.75}$ is slightly Tb-rich relative to the stoichimetric $Tb(Fe-Co)_2$ phase. Considering that the Tb-Fe-Co system behaves as a pseudo-binary Tb(Fe-Co), the alloy of the chosen composition would, under equilibrium solidification condition, display a two-phase microstructure consisting of $Tb(Fe-Co)_2$ and Tb-rich phases. Figure 1 shows the XRD patterns for the as-cast and melt spun $Tb(Fe_{0.55}Co_{0.45})_{1.75}$ ribbons prepared using two-wheel speeds, viz., 15 and 47 m/s. From X-ray diffraction studies, it is clear that the as-cast alloy and melt spun ribbons primarily consist of C15-type cubic Laves phase (SG: $Fd\bar{3}m$). In addition, the presence of a Tb-rich phase can also be observed. This is in concurrence with the binary Tb-Fe phase diagram which shows the presence of both these phases in the rare earth-rich compositions. The XRD patterns obtained from the melt spun ribbons exhibit shoulders around each of the major peaks of C15 Laves phase. Such shouldering is generally observed when a material undergoes high density of stacking faults while processing [25]. The high cooling rates of the melt spinning process is the likely cause of the formation of stacking faults in the melt spun ribbons.

Transmission electron micrographs for the rapidly solidified Tb-Fe-Co ribbons prepared at different wheel speeds are shown in Fig. 2. The bright-field TEM images (Fig. 2a, b, d) indicate a decrease in grain size with an increase in wheel speed. This essentially implies the formation of
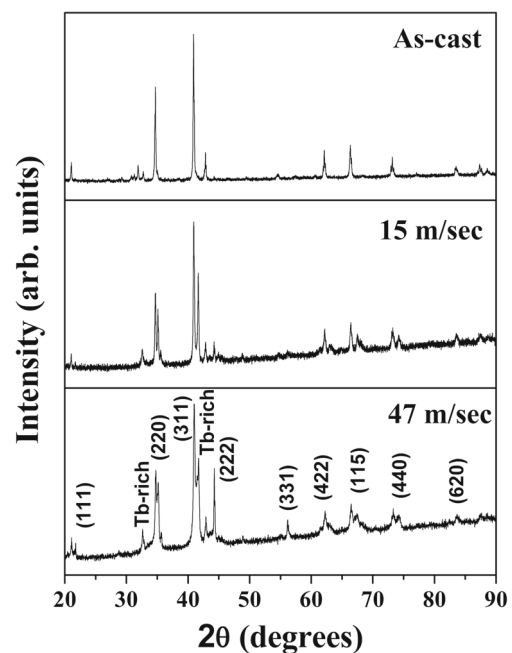

Fig. 1 XRD patterns of Tb-Fe-Co as-cast alloy and melt spun ribbons prepared at different wheel speeds
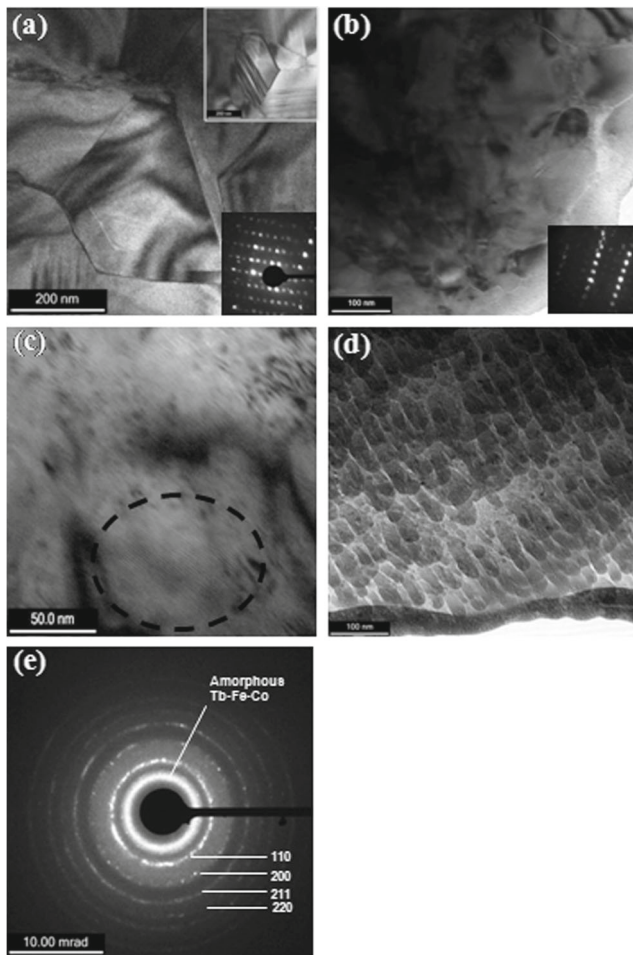
Fig. 2 Bright-field TEM images of samples melt spun at wheel speeds **a** 15 m/s (*insets*: SAD pattern and stacking faults formed during solidification), **b** 25 m/s (*inset*: SAD pattern and stacking faults formed during solidification), **c** 25 m/s showing a localized colony of BCC Fe-Co, and **d** 34 m/s. **e** The SAD pattern of the sample melt spun at 34 m/s wheel speed

finer grains at a higher solidification rate. The average grain size of the sample melt spun at 15 and 25 m/s is found

to be ∼200 and 100 nm, respectively (Fig. 2a, b). Occasionally, one can observe a formation of stacking faults (inset of Fig. 2a). The diffraction patterns (insets of Fig. 2a, b) predominantly indicate the formation of Tb(Fe-Co)$_2$ phase having the C15 Laves phase structure. In the sample melt spun at 25 m/s, occasional colonies of nano-crystalline BCC Fe-Co phase is also observed. However, as the wheel speed increases to 34 m/s, the microstructural investigation reveals the formation of BCC Fe-Co phase co-existing with amorphous Tb-Fe-Co. The selected area diffraction (SAD) pattern from the ribbon melt spun at 34 m/s rpm shows (Fig. 2e) a halo corresponding to amorphous Tb-Fe-Co and rings corresponding to nano-crystalline BCC Fe-Co phase. Such two-phase microstructure essentially occurs in samples melt spun at higher rpm owing to the formation of BCC Fe-Co phase as the primary phase solidified directly from the liquid. The volume fraction of the primary phase becomes sufficient in the sample melt spun at 34 m/s to make the neighboring liquid richer in Tb. Accordingly, the composition of the liquid shifts towards the eutectic point in Tb(Fe-Co) pseudo-binary phase diagram [26], which leads to the formation of amorphous Tb-Fe-Co under the influence of a high cooling rate. Similar phase segregations in sputter-deposited Tb-Fe-Co have been reported by Gao et al. [27]. However, it should be noted that the combination of BCC Fe-Co phase and amorphous Tb-Fe-Co is formed only in localized areas in the ribbon. The XRD pattern of the ribbon prepared at the same wheel speed shows crystalline Tb(Fe-Co)$_2$ as the major phase; it can be inferred that majority of the ribbon is crystallized as nano-crystalline Tb(Fe-Co)$_2$ (Fig. 1). The solidification sequence of the Tb-Fe-Co melt spun ribbons prepared with different wheel speeds is shown in Table 1.

Figure 3a, b shows the magnetization curves for the as-cast and melt spun Tb-Fe-Co ribbons at room temperature and at 5 K, respectively. The magnetization curves indicate that the magnetization is along the plane of the ribbon. From magnetization studies, it is evident that the as-cast sample exhibits a semi-hard behavior with a coercivity of

Table 1 Solidification sequence of the Tb-Fe-Co melt-spun ribbons prepared with different wheel speeds

15 m/s	25 m/s	≥ 34 m/s
L	L	L
↓	↓	↓
Tb(Fe-Co)$_2$ with extended solubility	BCC Fe-Co + L	BCC Fe-Co + L
	↓	↓
	BCC Fe-Co + Tb(Fe-Co)$_2$ with extended solubility	BCC Fe-Co + L + Tb(Fe-Co)$_2$ with extended solubility
		↓
		BCC Fe-Co + Tb(Fe-Co)$_2$ with extended solubility + amorphous Tb-Fe-Co

Fig. 3 Magnetization curves for as-cast and ribbons melt spun at different wheel speeds **a** at room temperature and **b** at low temperature
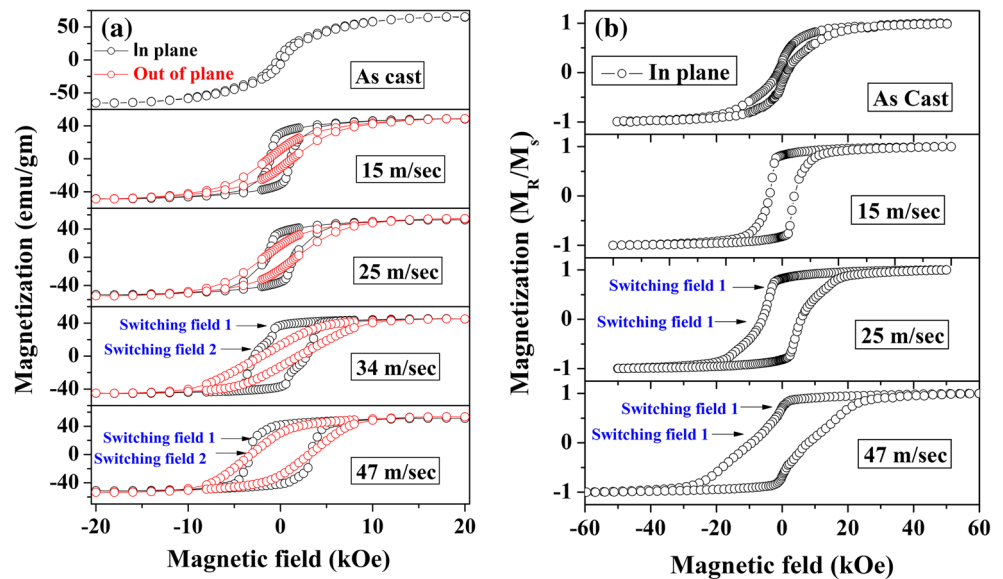
~300 Oe. Upon melt spinning, a considerable increase in the coercivity occurs both at room temperature and at low temperature. The enhanced coercivity values measured at a low temperature indicate the presence of strong anisotropy in the Tb-Fe-Co system. Further, it is observed that the coercivity at room temperature for Tb-Fe-Co ribbons measured along the in-plane and out-of-plane directions is nearly equal. The variation of coercivity measured for the as-cast alloy and ribbons prepared at different wheel speeds are listed in Table 2. The increase in the coercivity with an increase in wheel speed can be related to the decrease in the grain size which is clearly evidenced from the TEM studies (Fig. 2). In addition to a finer grain size, the formation of stacking faults also contributes to the increase in coercivity as observed from the TEM images of the melt spun ribbons (Inset of Fig. 2a). Further, it is worth mentioning also that there is a huge change in coercivity values for the ribbons prepared at higher wheel speeds (≥34 m/s) when compared with melt spun ribbons prepared at 15 and 25 m/s. This huge increase in the coercivity can be correlated to the formation of amorphous Tb-Fe-Co phase as indicated in the TEM microstructure (Fig. 2e). It has been well reported that amorphous Tb-Fe-Co alloys in thin film form is found to exhibit high coercivity owing to the large magnetic anisotropy [6, 10–13]. It is also interesting to note that

ribbons prepared at a higher wheel speed exhibit anisotropy along the out-of-plane direction which can also be attributed to the amorphization of Tb-Fe-Co phase (Fig. 4). The formation of amorphous Tb-Fe-Co is also evident from the small step (switching field) observed in the demagnetization curve (2nd quadrant of Fig. 3a), indicating the composite nature of the M-H loop (Fig. 3a). The presence of different magnetic components giving rise to two switching fields has also been earlier observed in phase-segregated Tb-Fe-Co films by Gao et al. [27].

Figure 5 shows the plots of electrical resistivity as a function of temperature in the range of 10–300 K for the as-cast and melt spun ribbons prepared at different wheel speeds, viz., 15, 25, and 34 m/s. The resistivity measurements for ribbons melt spun at a wheel speed of 47 m/s could not be carried out owing to the high brittleness of the ribbon. Figure 5 shows that in all cases the behavior is metallic.

In a ferromagnetic material, the temperature variation of resistivity has contributions from (i) residual resistivity (ρ_0), (ii) electron-electron scattering, (iii) electron-phonon scattering (ρ_{ph}), and (iv) electron-magnon scattering (ρ_{mag}). While the low-temperature resistivity is dominated by electron-electron scattering and electron-magnon scattering, electron-phonon scattering has a significant contribution to

Table 2 Variation of coercivity, residual resistivity and value of *A* for as-cast alloy and melt spun ribbons prepared with different wheel speeds

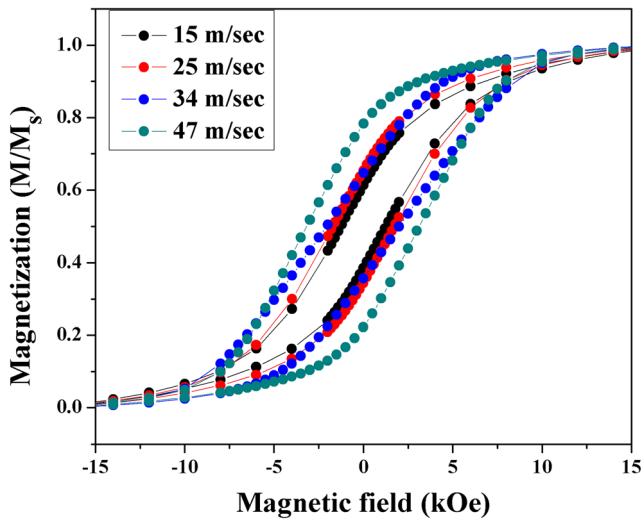| Processing parameter	Coercivity (kOe)	Residual resistivity, $\rho_0 (\mu\Omega\ cm)$	$A(n\Omega cm\ K^{-2})$
As-cast alloy	0.3	45	1.2
15 m/s	1.2	50	1.6
25 m/s	1.5	86	0.07
34 m/s	2.8	47	0.012
47 m/s	3.3	–	–

Fig. 4 Out-of-plane magnetization curves measured at room temperature for Tb-Fe-Co ribbons prepared at different wheel speeds

the resistivity at high temperatures. Therefore, at a low temperature, the resistivity is given by [28–30]

$$\rho(T) = \rho_0 + AT^2 \exp(-\Delta/KT) \quad (1)$$

where ρ_0 is the residual resistivity, A is a material-dependent constant, and Δ is the minimum energy required to excite magnons in the anisotropy field. In materials with high magnetocrystalline anisotropy, the energy required to excite magnons is very low. It has been reported that in HoFe$_2$, the energy for excitation of magnons is less

than 1 meV [31, 32]. Hence, the contribution from Δ can be neglected in Eq. (1) [28]. Therefore, the temperature dependence of resistivity at low temperatures for materials with high magneto-crystalline anisotropy is given as

$$\rho(T) = \rho_0 + AT^2. \quad (2)$$

From the fit, it is observed that the residual resistivity for the ribbons is substantially higher when compared with the as-cast values (Table 2). This could be attributed to the scattering of the electrons by the defects present in the materials such as grain boundaries, stacking faults, and vacancies. The presence of such grain boundaries and stacking faults in the ribbon has been seen from electron microscopy studies (inset of Fig. 2a, b). According to the Bloch model, at a low temperature, the periodic potential does not produce electrical resistance. However, deviations from perfect periodicity such as impurities, vacancies, grain boundaries, and dislocations lead to scattering of electrons yielding to finite residual resistivity ρ_0 at very low temperatures. This ρ_0 is independent of temperature.

The value of A in Eq. 2 is an indication of whether the electron-electron scattering or the electron-magnon scattering plays a significant role in the resistivity. If the electron-electron interaction is dominant, the value of A would be small (of the order of 2.5×10^{-2} nΩ cm K^{-2}), as in the case of pure Ni, where only electron-electron scattering is present at low temperatures. On the other hand, if the value of A is large (of the order of 5 nΩ cm K^{-2}), electron-magnon scattering dominates over the electron-electron scattering [28, 33]. The variation of residual resistivity and values of A for as-cast alloy and melt spun ribbons prepared at

Fig. 5 Temperature variation of resistivity for as-cast alloy and ribbons melt spun at different wheel speeds. *Solid lines* show the fit
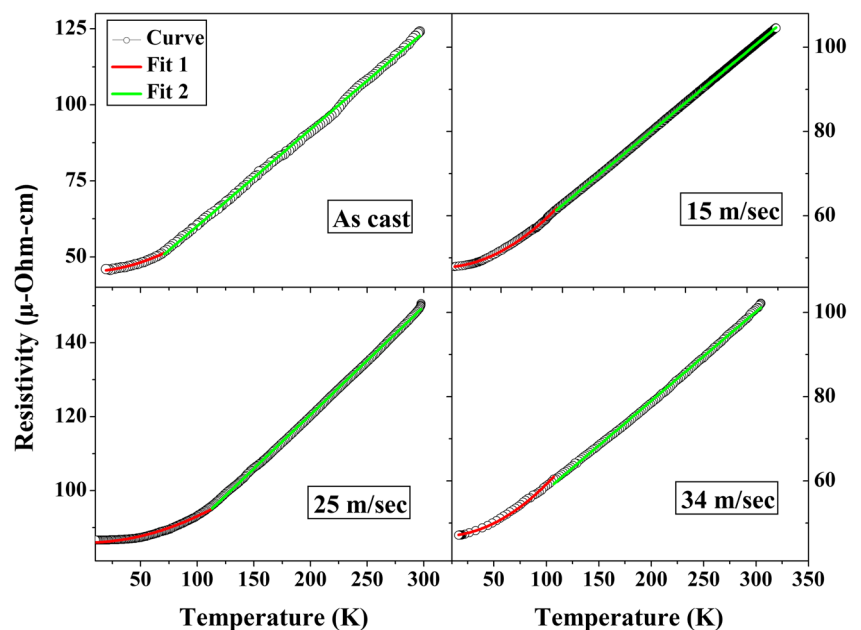
different wheel speeds are listed in the Table 2. The value of A for the as-cast alloy and ribbons melt spun at a wheel speed of 15 m/s is found to be 1.2 and 1.6 nΩ cm K^{-2}, respectively, suggesting that the electron-magnon scattering dominates as compared to electron-electron scattering mechanism. This is in concurrence with the results reported earlier on Mn added Tb-Dy-Fe alloys [26]. The value of A for the ribbons melt spun at 25 and 34 m/s wheel speed is found to be 7×10^{-2} and 1.2×10^{-2} nΩ cm K^{-2}, suggesting that for these ribbons electron-electron scattering is dominant. The possible reason for this is the evolution of various phases and the associated magnetism arising from these phases. The competition between the various magnetic phases such as amorphous Tb-Fe-Co, nano-crystalline Tb-Fe-Co, and Fe-Co phases with different anisotropies can evolve different spin-wave excitations which can annihilate the electron-magnon scattering.

4 Summary

Ribbons of Tb-Fe-Co alloy were prepared employing a vacuum melt spinner at different wheel speeds. The correlations obtained across the structure-microstructure-magnetic-electrical properties are summarized below:

(i) TEM studies indicate a decrease in the grain size with an increase in wheel speed owing to the higher solidification rates achieved.

(ii) Evolution of various phases (viz., C15-type crystalline Tb-Fe-Co, Fe-Co, and amorphous Tb-Fe-Co) could be evidenced from the ribbons prepared with different wheel speeds.

(iii) Coercivity measured from magnetization curves has been found to be significantly influenced by the grain size and defects induced during the melt spinning process. A maximum coercivity as high as 3.3 kOe has been achieved for the ribbon melt spun at 47 m/s.

(iv) Temperature-dependent electrical resistivity indicates a metallic behavior for the all the materials irrespective of the processing conditions. The residual resistivity evaluated from the temperature-dependent electrical resistivity measurement is found to be higher when compared with the as-cast alloy which is in compliance with the microstructural investigations. The low-temperature scattering mechanism is found to change from electro-magnon to electron-electron scattering for the ribbons prepared with higher wheel speeds.

References

1. Mansuripur, M.: Physical Principles of Magneto-Optical Recording. Cambridge University Press, Cambridge (1995)
2. Tsunashima, S.: J. Phys. D: Appl. Phys. **34**(17), R87 (2001)
3. Torii, Y., Wakiwaka, H., Kiyomiya, T., Matsuo, Y., Yamada, Y., Makimura, M.: J. Magn. Magn. Mater. **290–291**, 861 (2005)
4. Duc, N.H.: J. Magn. Magn. Mater. **242–245**, 1411 (2002)
5. Duc, N.H., Mackay, K., Betz, J., Givord, D.: J. Appl. Phys **79**, 973 (1996)
6. Umadevi, K., Bysakh, S., Arout Chelvane, J., Kamat, S.V., Jayalakshmi, V.: J. Alloys Compd. **663**, 430 (2016)
7. Basumatary, H., Arout Chelvane, J., Kamat, S.V., Ranjan, R.: J. Supercond. Nov. Magn. **29**, 863 (2016)
8. Anuniwat, N., Ding, M., Poon, S.J., Wolf, S.A., Lu, J.: J. Appl. Phys. **113**, 043905 (2013)
9. Gadetsky, S., Suzuki, T., Erwin, J.K., Mansuripur, M.: J. Magn. Soc. Jpn. **19**, 91 (1995)
10. Liu, Z., Zhou, S.M., Jiao, X.B.: J. Phys. D: Appl. Phys. **42**, 015008 (2009)
11. Brown, S., Harrell, J.W., Fujiwara, H., Takeuchi, T.: J. Appl. Phys **91**, 8243 (2002)
12. Basumatary, H., Arout Chelvane, J., Sridhara Rao, D.V., Kamat, S.V., Ranjan, R.: Thin Solid Films. **583**, 1 (2015)
13. Nakayama, M., Kai, T., Shimomura, N., Amano, M., Kitagawa, E., Nagase, T., Yoshikawa, M., Kishi, T., Ikegawa, S., Yoda, H.: J. Appl. Phys. **103**, 07A710 (2008)
14. Lee, C., Ye, L., Hsieh, T., Huang, C., Wu, T.: J. Appl. Phys **107**, 09C712 (2010)
15. Ohmori, H., Hatori, T., Nakagawa, S.: J. Appl. Phys. **103**, 07A911 (2008)
16. Duc, N.H., Huong Giang, D.T., Thuc, V.N., Minh Hong, N.T., Chau, N.: Physica B **327**, 328 (2003)
17. Leamy, H.J., Dirks, A.G.: J. Appl. Phys. **50**(4), 2871 (1979)
18. Sato, N.: J. Appl. Phys. **59**(7), 2514 (1986)
19. Harris, V.G., Aylesworth, K.D., Das, B.N., Elam, W.T., Koon, N.C.: Phys. Rev. Lett. **69**(13), 1939 (1992)
20. Li, G., Smith, D.J., Sickafus, K.: Appl. Phys. Lett. **55**, 919 (1989)
21. Rahman, T., Liu, X., Morisako, A., Matsumoto, M.: J. Magn. Magn. Mater. **287**, 250 (2005)
22. Sato, J., Murakami, Y., Fuji, H., Kojima, K., Takahashi, A., Nakatani, R., Yamamoto, M.: Jpn. J. Appl. Phys. **47**(1), 150 (2008)
23. Fang, Y.H., Kuo, P.C., Chou, C.Y., Chen, S.C., Cheng, N.W., Lin, P.L.: J. Magn. Magn. Mater. **310**, e930 (2007)
24. Yin, S.Q., Li, X.Q., Xu, X.G., Miao, J., Jiang, Y.: IEEE Trans. Magn. **47**(10), 3129 (2011)
25. Balogh, L., Ribárik, G., Ungár, T.: J. Appl. Phys. **100**, 023512 (2006)
26. Palit, M., Pandian, S., Chattopadhyay, K.: J. Alloys Compd. **541**, 297 (2012)
27. Gao, T.R., Xu, X.Y., Zhou, S.M., Li, J., Xia, A.-L., Han, B.-S.: J. Magn. Magn. Mater. **306**, 324 (2006)
28. Mannari, L.: Prog. Theor. Phys. **22**, 335 (1959)
29. Arout Chelvane, J., Markandeyulu, G.: J. Magn. Magn. Mater. **294**, 298 (2005)
30. Mackintosh, A.R.: Phys. Lett. **4**, 140 (1963)
31. Gratz, E., Zuckerman, M.J.: In: Kschneidner, K.A., Eyring, L. (eds.) Hand book of physics and chemistry of rare earths, p. 117. North Holland, Amsterdam (1982). (chapter 42)
32. Rhyne, J.J., Koon, N.C.: J. Appl. Phys. **49**, 2133 (1978)
33. Suresh, K.G., Rama Rao, K.V.S.: J. Alloys Compounds **238**, 90 (1996)